Single-Phase Independent Model Predictive Control for Open-End Winding Motor Fed by Dual Three-Level Inverters

Chao LUO, Guifeng WANG, Qigang DU, Jinling JI, Weipeng SHI, and Ke LI

***Abstract*—For open-end winding induction motor (OEWIM) fed by dual three-level inverters, traditional model predictive current control (MPCC) suffers from issues such as excessive vector enumeration, complex control algorithm design, and slow dynamic response. This paper proposes a low voltage jump single-phase independent model predictive current control (LVJ-SPI-MPCC) method. Firstly, by establishing a single-phase independent predictive current model, the independent prediction and optimization of the switching states for each phase leg are achieved, reducing the number of optimal switching state selections per control cycle from 729 to 27. Secondly, to suppress phase voltage jumps, a switching state selection rule based on a voltage jump constraint is proposed, constructing a collaborative optimization strategy for low voltage jump and single-phase independent control. This limits the phase voltage jump within the range of $\pm U_{dc}/2$ and further reduces the predictive computations per cycle to 15. Finally, the effectiveness of the proposed method is verified based on MATLAB/Simulink simulations and the Typhoon HIL 402 experimental platform. Experimental results show that the proposed method significantly reduces the computational burden and improves the system's dynamic response speed while ensuring control accuracy.**

***Index Terms*—Dual three-level inverter, low voltage jump, open-end winding induction motor, single-phase independent model predictive current control.**

I. Introduction

With the rapid development of industrial automation, new energy vehicles, and renewable energy, more stringent technical requirements are imposed on the dynamic response characteristics, control accuracy, and operational reliability of motor drive systems. Traditional induction motors powered by a single inverter face significant challenges due to their inherent topology, such as limited voltage output capability, insufficient current harmonic suppression, and weak system fault tolerance. Open-end winding induction motor, with their dual-inverter supply topology, offer advantages like multi-level voltage output, high voltage utilization, and fault-tolerant operation, making them a research hotspot in the field of motor control in recent years [1], [2]. Compared to single-ended supply systems, dual-inverter systems can provide higher output voltage and more phase voltage levels [3], and avoid issues related to voltage balancing in traditional series-connected switching devices [4].

Dual-inverter topologies are mainly divided into common DC-bus and isolated DC-bus structures based on the bus connection method [5], [6]. Compared to the common DC-bus structure, the isolated DC-bus structure uses two independent DC sources. Although it has higher cost and more complex control, its rectifier parts are isolated from each other, which can effectively solve the inherent zero-sequence circulating current problem in dual-inverter topologies [7], [8], thus avoiding the zero-sequence current issue present in common DC-bus structures.

Currently, research on control methods for open-end winding motors is deepening, and various high-performance control strategies have been developed, not only improving the dynamic performance of the motor but also expanding its application scenarios. These mainly include vector control [9], direct torque control (DTC) [10], model predictive control (MPC) [11], and several other high-performance control strategies.

Although vector control technology is widely used in industry due to its precise control capability and fast dynamic response, several defects have been found in practical applications: Firstly, the calculation process involved in coordinate transformation is relatively complex. Secondly, the control algorithm highly depends on the accuracy of motor parameters. Finally, system performance is susceptible to parameter measurement errors [12]. Direct torque control also has some shortcomings, particularly the potential for flux ripple in low-speed operating regions. Furthermore, its implementation requires high hardware support to ensure precise current control and state calculation at high frequencies [13].

With the advancement of microprocessor technology, model predictive control (MPC) has gradually emerged in the field of

Manuscript received September 10, 2025; revised November 21, 2025; accepted December 11, 2025. Date of publication March 30, 2026; date of current version February 2, 2026. This work was supported in part by the Project of Universities in Xuzhou Serving the Development of the "343" Industries under the grant GX2024009. (*Corresponding author: Weipeng Shi*.)

C. Luo, G. Wang, Q. Du, J. Ji, and W. Shi are with the School of Electrical Engineering and Automation, Jiangsu Normal University, Xuzhou 221116, China (e-mail: 2020231837@jsnu.edu.cn; 6020160105@jsnu.edu.cn; 2020231815@jsnu.edu.cn; 2020231803@jsnu.edu.cn; shiweipeng@jsnu.edu.cn).

K. Li is with the Xuzhou Nanpu Electromechanical Technology Co., Ltd., Xuzhou 221600, China (e-mail: 1444538580@qq.com).

Digital Object Identifier 10.24295/CPSSTPEA.2025.00044

power electronics and is widely used for controlling AC motors and converters [14], [15]. MPC can be categorized based on predicted quantities or cost functions into model predictive torque control (MPTC), model predictive flux control (MPFC), and model predictive current control (MPCC), etc. [16]–[19]. However, due to the large number of switches in the dual-inverter structure, traditional MPC schemes suffer from high control complexity. Some studies have applied MPC to dual-converter systems with isolated power supplies, adopting the weighting factor-free scheme from single-converter model predictive control [20], eliminating weighting factors in the cost function and reducing algorithm complexity. [21] proposed an improved weightless model predictive torque control method, effectively reducing computational complexity and low-order current harmonics by defining an improved control set. [22] proposed an improved MPC method for zero-sequence current suppression, using a deadbeat predictive model to determine the optimal voltage vector, significantly improving control performance and increasing DC bus voltage utilization. Lakhimsetty et al. proposed an improved predictive current control strategy for a four-level open-end winding induction motor drive fed by a dual inverter. By fixing the inverter with the lower DC input voltage and switching the other, the evaluated voltage vectors were reduced from 37 to 5, effectively reducing the controller's computational burden and switching frequency while performing excellently in terms of voltage and current total harmonic distortion (THD), torque ripple, and total drive losses [23]. Gao Fengyang et al. introduced an active disturbance rejection cascaded model predictive current control method, successfully avoiding the tuning of weighting coefficients in traditional model predictive control by hierarchically optimizing *d-q* axis currents, zero-sequence current, and switching frequency [24]. [25] used a voltage-based control method instead of current-based control to reduce the number of MPC calculations, achieving high computational efficiency, and utilized the reduced computational burden to decrease sampling time, obtaining excellent drive performance. However, the aforementioned methods are all based on the topology of OEWIMs driven by dual two-level inverters. If applied to the dual three-level inverter drive scheme adopted in this paper, the computational load would increase exponentially [26]. Traditional finite-control-set (FCS)-MPCC requires enumerating all switching vector combinations. For dual threelevel inverters, 27×27 = 729 switching combinations need to be evaluated, making it difficult to meet real-time requirements.

To effectively solve the problem of high computational load in traditional model predictive current control for open-end winding induction motor (OEWIM) driven by dual three-level inverters, this paper proposes a low voltage jump single-phase independent model predictive current control (LVJ-SPI-MPCC) method. By establishing a single-phase independent predictive current model, independent prediction and optimization of the switching states for each phase leg are achieved. A collaborative optimization strategy for low phase voltage jump and single-phase independent control is constructed, reducing the number of optimal switching state selections per control cycle from 729 to 15.

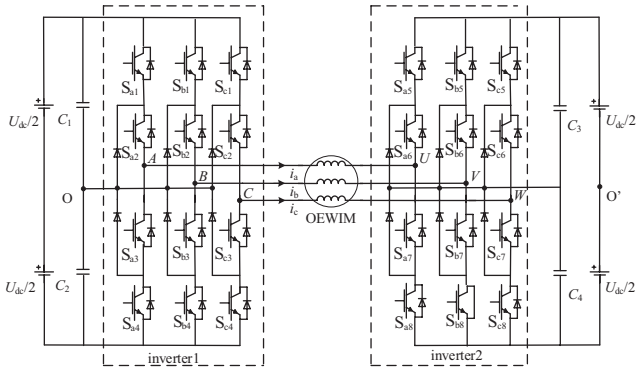

Fig. 1. Circuit diagram of an OEWIM fed by dual three-level inverters with isolated DC bus structure.

II. OEWIM Model Based on Dual Three-Level Inverter

A. Mathematical Model of OEWIM

The topology of the OEWIM fed by dual three-level inverters is shown in Fig. 1. The two inverters are powered by two sets of DC power supplies respectively. This topology breaks the path for zero-sequence current, so no zero-sequence current exists.

According to Fig. 1, the three-phase leg switching states of the dual three-level inverter OEWIM topology are:

$$\begin{cases} S_{AU} = S_{a1} + S_{a2} - S_{a3} - S_{a4} - S_{a5} - S_{a6} + S_{a7} + S_{a8} \\ S_{BV} = S_{b1} + S_{b2} - S_{b3} - S_{b4} - S_{b5} - S_{b6} + S_{b7} + S_{b8} \\ S_{CW} = S_{c1} + S_{c2} - S_{c3} - S_{c4} - S_{c5} - S_{c6} + S_{c7} + S_{c8} \end{cases} \quad (1)$$

In (1), S_{AU}, S_{BV}, S_{CW} are the three-phase switching functions of the inverters, where S_{a1}–S_{a8}, S_{b1}–S_{b8}, S_{c1}–S_{c8} are the switching states of the inverter switching devices, taking values of 0 or 1.

According to Fig. 1, the three-phase output phase voltages of the dual three-level inverter OEWIM topology are:

$$\begin{cases} u_{AU} = u_{AO} - u_{UO'} = \dfrac{U_{dc}}{2} S_{AU} \\ u_{BV} = u_{BO} - u_{VO'} = \dfrac{U_{dc}}{2} S_{BV} \\ u_{CW} = u_{CO} - u_{WO'} = \dfrac{U_{dc}}{2} S_{CW} \end{cases} \quad (2)$$

where, u_{AU}, u_{BV}, and u_{CW} are the three-phase output phase voltages of the dual three-level inverter OEWIM topology.

The correspondence between the output switching states and output voltages for a single phase of the dual three-level inverter OEWIM is shown in Table I. The dual three-level inverter system can output 9 switching states in total, corresponding to 5 output voltage levels.

Based on the analysis of the output voltage states between single-phase windings of the OEWIM, and to simplify the

TABLE I
SINGLE-PHASE OUTPUT STATE, OUTPUT VOLTAGE, AND SWITCHING STATE FOR DUAL THREE-LEVEL INVERTER OEWIM

Inverter 1-output		Inverter 2-output		Dual three-level		Inverter-output
State	Voltage	State	Voltage	State	Voltage	Switching state
1	$U_{dc}/2$	−1	$-U_{dc}/2$	2	U_{dc}	S_1
1	$U_{dc}/2$	0	0	1	$U_{dc}/2$	S_2
0	0	−1	$-U_{dc}/2$	1	$U_{dc}/2$	S_3
1	$U_{dc}/2$	1	$U_{dc}/2$	0	0	S_4
0	0	0	0	0	0	S_5
−1	$-U_{dc}/2$	−1	$-U_{dc}/2$	0	0	S_6
−1	$-U_{dc}/2$	0	0	−1	$-U_{dc}/2$	S_7
0	0	1	$U_{dc}/2$	−1	$-U_{dc}/2$	S_8
−1	$-U_{dc}/2$	1	$U_{dc}/2$	−2	$-U_{dc}$	S_9

modeling process, when the motor is running, the OEWIM stator current is taken as the control object. In the *d-q* coordinate system, setting the *d*-axis along the rotor flux direction means the *q*-axis component of the rotor flux is always zero. The state equation of the OEWIM mathematical model is:

$$\begin{cases} \dfrac{\mathrm{d}\psi_{rd}}{\mathrm{d}t} = -\dfrac{1}{T_r}\psi_{rd} + \dfrac{L_m}{T_r} i_{sd} \\ \dfrac{\mathrm{d}i_{sd}}{\mathrm{d}t} = \dfrac{k_r}{\delta L_r T_r}\psi_{rd} - \dfrac{r_o}{\delta L_s} i_{sd} + \omega_e i_{sq} + \dfrac{1}{\delta L_s} u_{sd} \\ \dfrac{\mathrm{d}i_{sq}}{\mathrm{d}t} = -\dfrac{n_p k_r \omega}{\delta L_r}\psi_{rd} - \dfrac{r_o}{\delta L_s} i_{sq} - \omega_e i_{sd} + \dfrac{1}{\delta L_s} u_{sd} \end{cases} \tag{3}$$

where i_{sd}, i_{sq} and u_{sd}, u_{sq} are the stator currents and stator voltages on the *d*- and *q*-axis respectively, Ψ_{rd} is the *d*-axis rotor flux, R_s is the stator resistance, R_r is the rotor resistance, L_r, L_s are the rotor and stator inductances respectively, L_m is the mutual inductance, ω_e is the synchronous speed, ω is the rotor speed, n_p is the number of pole pairs. $T_r = L_r/R_r$ is the rotor electromagnetic time constant, $k_r = L_m/L_r$, $r_o = R_s + R_r k_r^2$, $\delta = 1 - L_m^2/L_s/L_r$.

B. Space Vector Distribution of OEWIM

According to the definition of voltage space vectors, the voltage space vector diagram of the dual three-level inverter OEWIM can be drawn, as shown in Fig. 2. In the figure, the numbers inside the circles correspond to the number of switching states for each voltage vector. For example, the number 36 indicates that this voltage vector has 36 switching states. Referring to Table I, the numbers outside the circles correspond to the three-phase output states of the dual three-level inverter topology. For example, the three-phase output state 0, −2, 1 corresponds to output voltages of 0, $-U_{dc}$, and $-U_{dc}/2$. The dual three-level inverter has 125 voltage vectors, achieving control effects similar to a five-level inverter. However, compared to the 125 switching states of a traditional five-level inverter, the dual three-level inverter has 729 switching states. Therefore, using traditional FCS-MPCC for

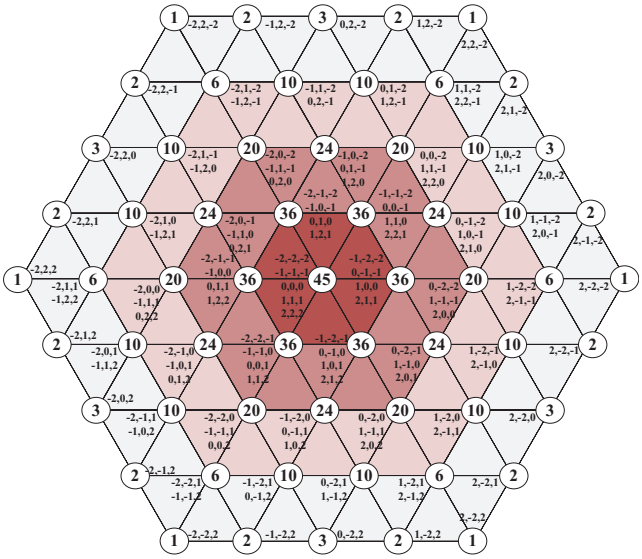

Fig. 2. Space voltage vector diagram of the dual three-level inverter.

switching state optimization suffers from excessive predictive computation and slow system response.

C. Traditional FCS-MPCC Method

The FCS-MPCC algorithm employs the dynamic model of the controlled system for predictive control. By integrating relevant system variable information obtained at the current and past sampling instants, it predicts the output trajectory of the controlled object or process over a future time horizon, thereby providing anticipatory information for the control system. On this basis, a cost function is constructed. Through online optimization, the optimal control input sequence for the system is selected, driving the output trajectory of the controlled object to approach or even achieve the reference trajectory, thus accomplishing the goal of optimal system control.

First, the prediction model of the OEWIM system is analyzed, and the corresponding cost function is selected. Discretizing the voltage equation in (3) using the forward Euler method, the current prediction model in the *d-q* coordinate system for the open-end winding motor control system is obtained:

$$\begin{cases} i_{sd}^{k+1} = (1 - \dfrac{T_s r_o}{\delta L_s}) i_{sd}^k + \dfrac{T_s k_r}{\delta L_r T_r}\psi_{rd}^k + T_s \omega_e i_{sq}^k + \dfrac{T_s}{\delta L_s} u_{sd}^k \\ i_{sq}^{k+1} = (1 - \dfrac{T_s r_o}{\delta L_s}) i_{sq}^k - \dfrac{T_s n_p k_r \omega}{\delta L_r}\psi_{rd}^k - T_s \omega_e i_{sd}^k + \dfrac{T_s}{\delta L_s} u_{sd}^k \end{cases} \tag{4}$$

where k denotes the current moment, k+1 is the next moment state.

The cost function is then expressed as:

$$g_{(i)} = [i_{sd\mathrm{ref}(i)} - i_{sd(i)}]^2 - [i_{sq\mathrm{ref}(i)} - i_{sq(i)}]^2 \tag{5}$$

where $i = [1, 719]$, $i_{sd\mathrm{ref}}$, $i_{sq\mathrm{ref}}$ are the given *d*-axis stator current and *q*-axis stator current respectively. The above cost function compares the error between the predicted current and the

reference current, and selects the switching state that minimizes the cost function value through enumeration.

III. Low Voltage Jump Single-Phase Independent Model Predictive Control Method for Dual Three-Level Inverter

A. LVJ-SPI-MPCC Method for Dual Three-Level Inverter

The single-phase independent model predictive model is based on the voltage and current mathematical model of the open-end winding induction motor in the three-phase stationary coordinate system. It controls the motor system by predicting the state of each phase of the OEWIM and the output of the dual three-phase currents.

The specific implementation steps of the proposed SPI-MPCC method are as follows: First, sample the motor's current, speed, and flux at time k, and convert these parameters into parameters in the d-q coordinate system. Secondly, subtract the actual observed flux from the given flux value, and obtain the d-axis stator current reference value through a PI regulator; Then, compare the given speed with the actual speed, and obtain the q-axis stator current reference value through a PI regulator; Next, transform the stator current reference values through inverse Park and inverse Clark transformations to obtain the current reference values in the three-phase stationary coordinate system. Finally, substitute the obtained predicted current values and current reference values into the cost function for comparison, select the predicted current value that minimizes the cost function, and output its corresponding switching vector.

The voltage and current equations of the open-end winding induction motor in three-phase stationary coordinate system are:

$$\begin{cases} u_{\mathrm{A}} = R_{\mathrm{s}} i_{\mathrm{A}} + L_{\mathrm{s}} \dfrac{\mathrm{d}i_{\mathrm{A}}}{\mathrm{d}t} + L_{\mathrm{m}} \dfrac{\mathrm{d}i_{\mathrm{B}}}{\mathrm{d}t} + L_{\mathrm{m}} \dfrac{\mathrm{d}i_{\mathrm{C}}}{\mathrm{d}t} \\ u_{\mathrm{B}} = R_{\mathrm{s}} i_{\mathrm{B}} + L_{\mathrm{s}} \dfrac{\mathrm{d}i_{\mathrm{B}}}{\mathrm{d}t} + L_{\mathrm{m}} \dfrac{\mathrm{d}i_{\mathrm{A}}}{\mathrm{d}t} + L_{\mathrm{m}} \dfrac{\mathrm{d}i_{\mathrm{C}}}{\mathrm{d}t} \\ u_{\mathrm{C}} = R_{\mathrm{s}} i_{\mathrm{C}} + L_{\mathrm{s}} \dfrac{\mathrm{d}i_{\mathrm{C}}}{\mathrm{d}t} + L_{\mathrm{m}} \dfrac{\mathrm{d}i_{\mathrm{A}}}{\mathrm{d}t} + L_{\mathrm{m}} \dfrac{\mathrm{d}i_{\mathrm{B}}}{\mathrm{d}t} \\ u_{\mathrm{A}} + u_{\mathrm{B}} + u_{\mathrm{C}} = 0 \end{cases} \tag{6}$$

Discretizing (6) using the forward Euler method, the mathematical model for predicting the three-phase current values of each inverter at time $k+1$ is obtained:

$$\begin{cases} i_{\mathrm{A}}(k+1) = i_{\mathrm{A}}(k) - \dfrac{T_{\mathrm{S}}}{L_{\mathrm{m}} - L_{\mathrm{s}}} [u_{\mathrm{A}} - R_{\mathrm{s}} \cdot i_{\mathrm{A}}(k)] \\ i_{\mathrm{B}}(k+1) = i_{\mathrm{B}}(k) - \dfrac{T_{\mathrm{S}}}{L_{\mathrm{m}} - L_{\mathrm{s}}} [u_{\mathrm{B}} - R_{\mathrm{s}} \cdot i_{\mathrm{B}}(k)] \\ i_{\mathrm{C}}(k+1) = i_{\mathrm{C}}(k) - \dfrac{T_{\mathrm{S}}}{L_{\mathrm{m}} - L_{\mathrm{s}}} [u_{\mathrm{C}} - R_{\mathrm{s}} \cdot i_{\mathrm{C}}(k)] \end{cases} \tag{7}$$

where $i_{\mathrm{A}}(k)$, $i_{\mathrm{B}}(k)$, and $i_{\mathrm{C}}(k)$ are the currently measured three-phase current values, $i_{\mathrm{A}}(k+1)$, $i_{\mathrm{B}}(k+1)$, and $i_{\mathrm{C}}(k+1)$ are the predicted current values for the next moment, T_{S} represents one control period.

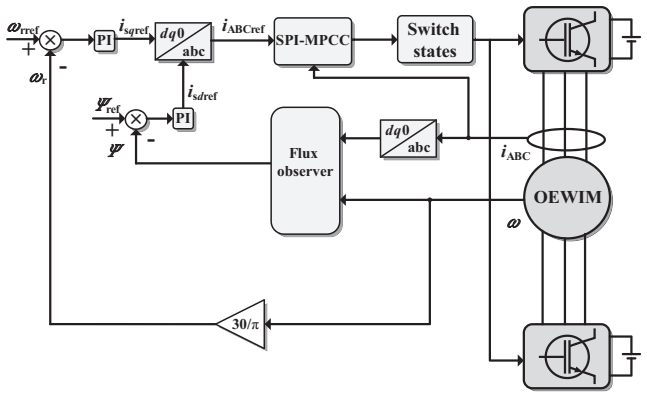

Fig. 3. Block diagram of the single-phase independent model predictive control method for the dual three-level inverter OEWIM.

Establish the single-phase independent model predictive cost function:

$$\begin{cases} g_{\mathrm{A}(j)} = [i_{\mathrm{A}(j)}(k+1) - i_{\mathrm{A}(j)\mathrm{ref}}]^2 \\ g_{\mathrm{B}(j)} = [i_{\mathrm{B}(j)}(k+1) - i_{\mathrm{B}(j)\mathrm{ref}}]^2 \\ g_{\mathrm{C}(j)} = [i_{\mathrm{C}(j)}(k+1) - i_{\mathrm{C}(j)\mathrm{ref}}]^2 \end{cases} \tag{8}$$

Where, j = [1, 9]. Substitute the obtained predicted current values and current reference values into the cost function for comparison, select the predicted current value that minimizes the cost function, and output its corresponding switching vector.

The control block diagram of the single-phase independent model predictive control method for the dual three-level inverter OEWIM is shown in Fig. 3.

The proposed method combines the model predictive control method for dual three-level open-end winding motors with the idea of single-phase independent control. It changes the need to enumerate and optimize all switching states of the six legs within a single sampling period to only needing to optimize the effective working states of each phase separately within a single sampling period. The predictive computation is reduced from 729 calculations to 27 calculations, significantly reducing the computational load while ensuring good control performance.

B. Voltage Jump Suppression Rule

The inverter has the problem of high voltage jumps when outputting AC side voltage. High voltage jumps can cause severe electromagnetic interference and harm motor equipment. Therefore, voltage jumps need to be constrained:

$$|S_x(k+1) - S_x(k)| \leqslant 1 \tag{9}$$

where, x = [A, B, C].

(9) can limit the phase voltage jump within $U_{\mathrm{dc}}/2$. The switching state transition rules for the dual three-level inverter

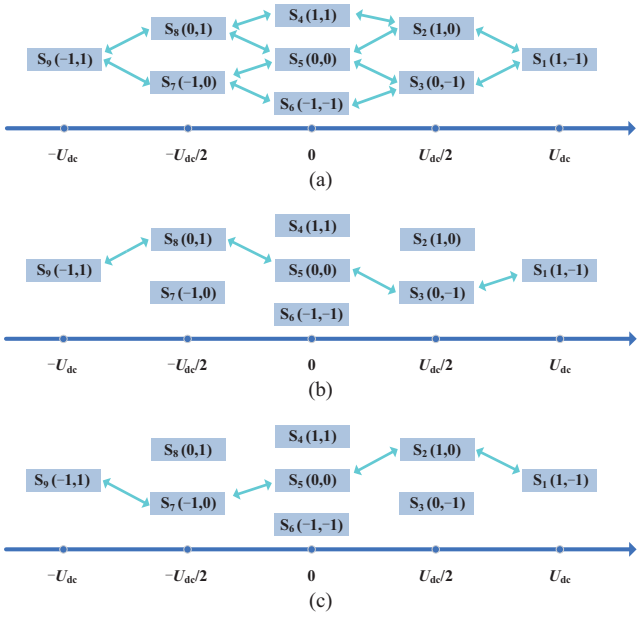

Fig. 4. Low voltage jump switching transition rules. (a) Low-voltage jumper switch switching diagram, (b) Low-voltage jumper switch switching diagram for zero-level output of inverter 1, (c) Low-voltage jumper switch switching diagram for zero-level output of inverter 2.

OEWIM are shown in Fig. 4(a).

To eliminate redundant switching states and further reduce computational load, the switching state selection rule is optimized. S_5 can switch with S_2, S_3, S_7, S_8. Therefore, at the 0 level, only switching state S_5 is retained, and redundant switching states S_4, S_6 are eliminated. There are two ways to select switching states at the $\pm U_{dc}/2$ levels. When the phase voltage switches between $-U_{dc}/2$ and $U_{dc}/2$, if inverter 1 is kept outputting 0 level during the switch, then redundant switching states S_2, S_4, S_6, S_7 are eliminated, retaining S_1, S_3, S_5, S_8, S_9, and the switching state transition rule shown in Fig. 4(b) is selected; If inverter 2 is kept outputting 0 level, then the switching state transition rule shown in Fig. 4(c) is selected. Thus, each phase only needs 5 enumerations, reducing the overall computation from 27 to 15.

The specific flowchart for switching state selection is shown in Fig. 5. After applying the voltage jump constraint and low switching loss state selection, the switching state with the optimal current tracking effect is chosen.

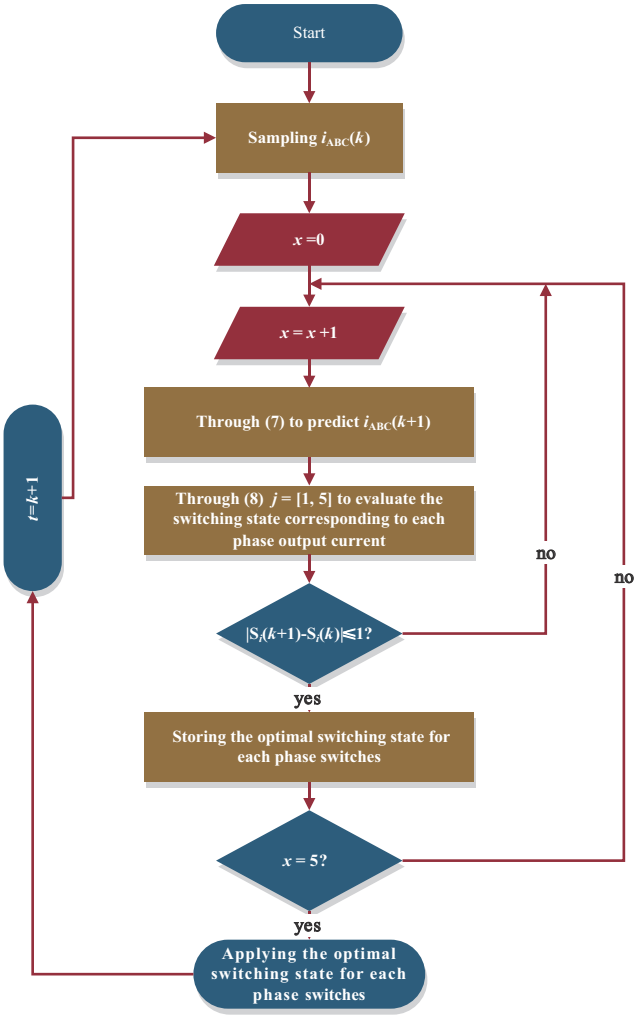

Fig. 5. LVJ-SPI-MPCC control flowchart.

TABLE II
OPEN-END WINDING INDUCTION MOTOR PARAMETERS

Parameter	Value	Parameter	Value
Rated voltage	380 V	Rotor resistance	1.91 Ω
Rated burrent	11.8 A	Stator resistance	1.45 Ω
Rated power	4.5 kW	Stator/rotor inductance	0.249 H
Rated speed	1420 r/min	Mutual inductance	0.235 H
Rated torque	30 N·m	Number of pole pairs	2

IV. SIMULATION AND EXPERIMENTAL RESULT ANALYSIS

To verify the effectiveness of the proposed LVJ-SPI-MPCC strategy for the OEWIM driven by the dual three-level inverter, simulations and experimental analyses were conducted using Matlab/Simulink and a platform based on DSP+FPGA+Typhoon HIL 402. The OEWIM simulation parameters are shown in Table II. The DC side voltage U_{dc} is set to 400 V, T_S is set to 100 μs.

A. Simulation Result Analysis

This paper compares and analyzes the proposed LVJ-SPI-MPCC with traditional MPCC under different operating conditions to verify the control performance of the proposed method. Simulations were first conducted at low speed 500 r/min, medium speed 1000 r/min, and rated speed 1420 r/min with rated load 30 N·m applied.

Fig. 6 shows the simulation comparison between traditional FCS-MPCC and LVJ-SPI-MPCC under low-speed conditions 500 r/min. The motor was started at no-load at 0 s, and the rated load was applied at 1 s. The simulation results show that the torque regulation time T_{rs} was 0.081 s for traditional FCS-MPCC, while it was shortened to 0.05 s for LVJ-SPI-MPCC. Furthermore, LVJ-SPI-MPCC exhibited smaller

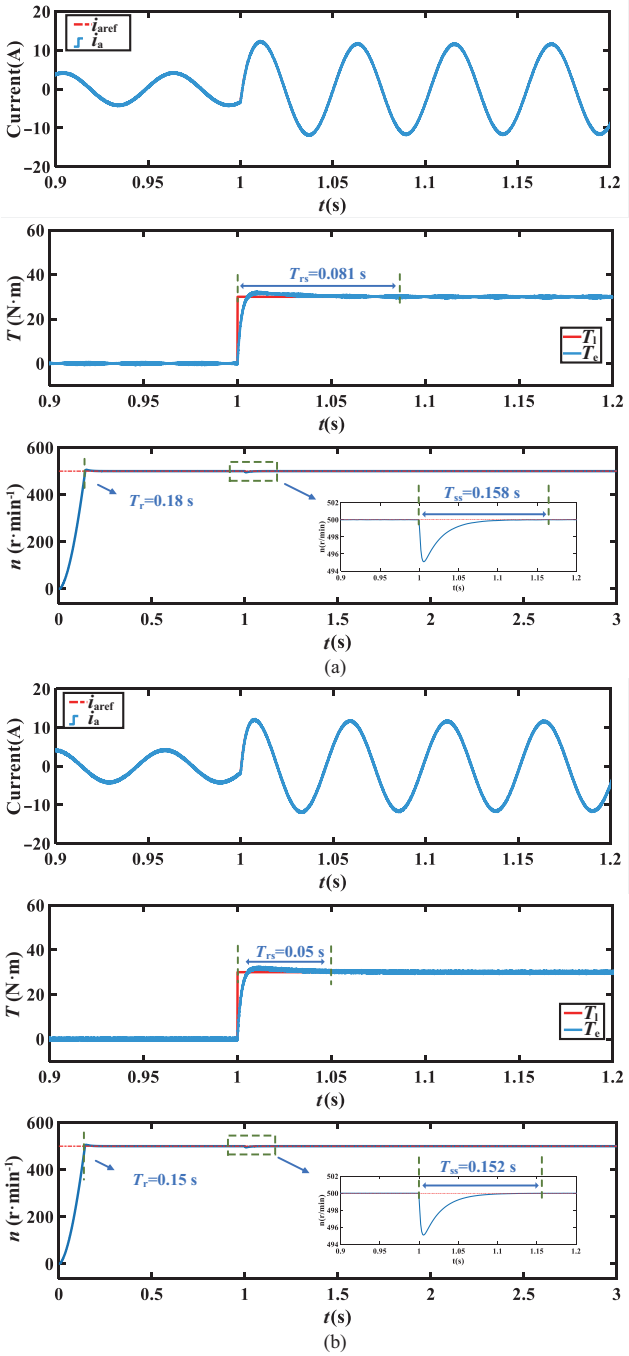

Fig. 6. Simulation comparison under low-speed condition 500 r/min. (a) Traditional FCS-MPCC, (b) LVJ-SPI-MPCC.

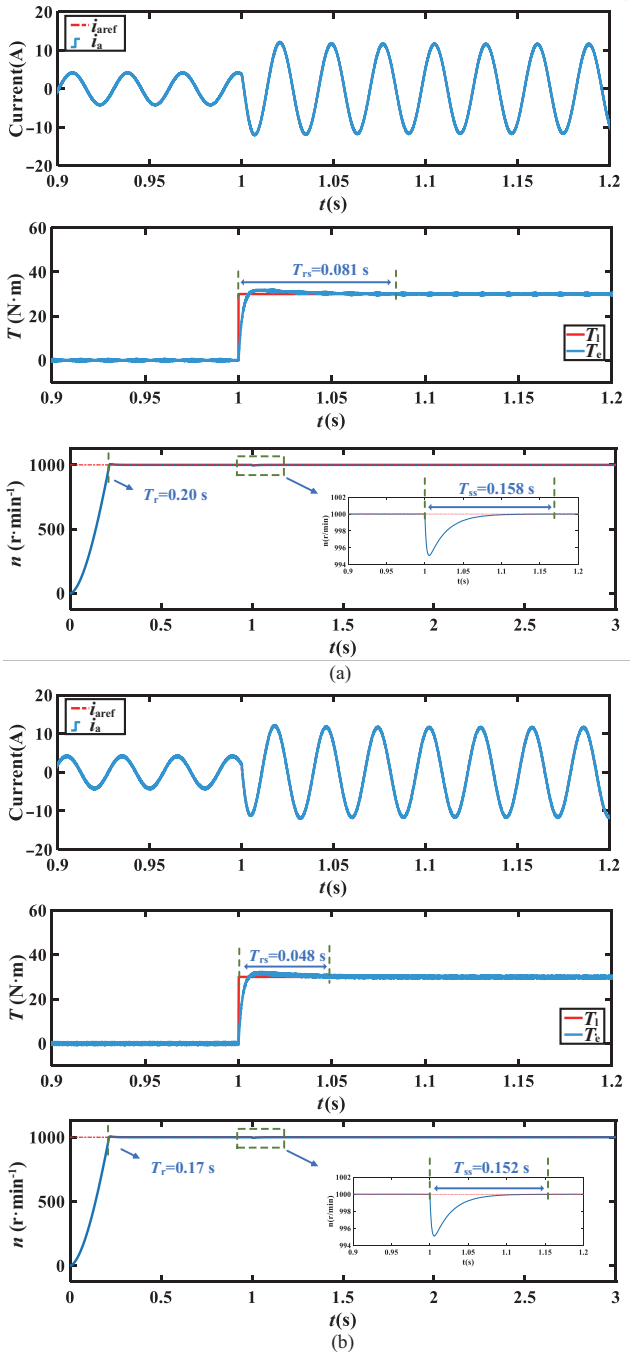

Fig. 7. Simulation comparison under medium-speed condition 1000 r/min. (a) Traditional FCS-MPCC, (b) LVJ-SPI-MPCC.

torque overshoot and achieved stable torque more rapidly and smoothly. The speed rise time T_r was 0.18 s for traditional FCS-MPCC, and the settling time after load application T_{ss} was 0.158 s. In contrast, LVJ-SPI-MPCC reduced T_r to 0.15 s and T_{ss} to 0.152 s. Compared to traditional FCS-MPCC, LVJ-SPI-MPCC reduced the torque regulation time by approximately 38.3%, the speed rise time by 16.7%, and the speed fluctuation settling time by approximately 3.8%.

Similarly, when operating at the medium speed of 1000 r/min, the motor was started at no-load at 0 s and the rated load was applied at 1 s. The simulation comparison is shown in Fig. 7. Under LVJ-SPI-MPCC, the phase current accurately tracked the reference current, with smooth and stable waveforms. The torque regulation time T_{rs} was 0.081 s for traditional FCS-MPCC but was reduced to 0.048 s with LVJ-SPI-MPCC, which also exhibited smaller overshoot. The speed rise and stable operation response time T_r was 0.20 s for traditional FCS-MPCC, which was shortened to 0.17 s with LVJ-SPI-MPCC. The speed regulation time after load application T_{ss} was reduced from 0.158 s to 0.152 s. Compared to traditional FCS-MPCC, LVJ-SPI-MPCC reduced the torque regulation time by approximately 40.7%, the speed rise time by 15.0%,

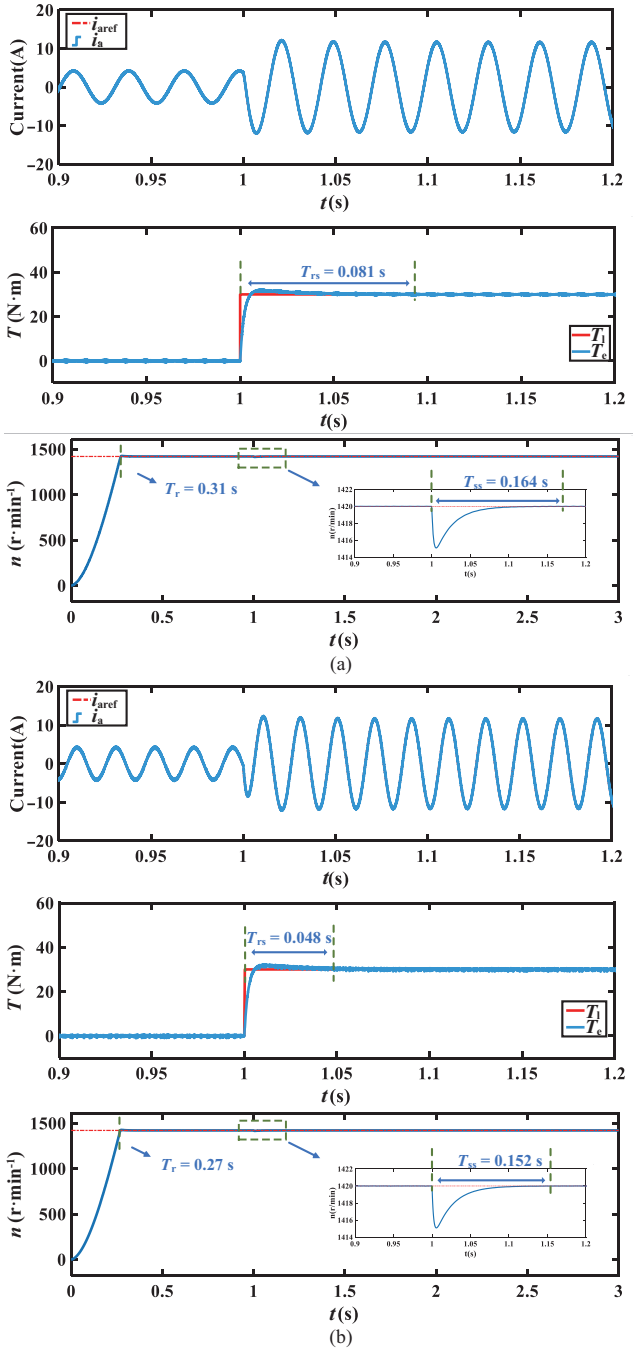

Fig. 8. Simulation comparison under rated condition. (a) Traditional FCS-MPCC, (b) LVJ-SPI-MPCC.

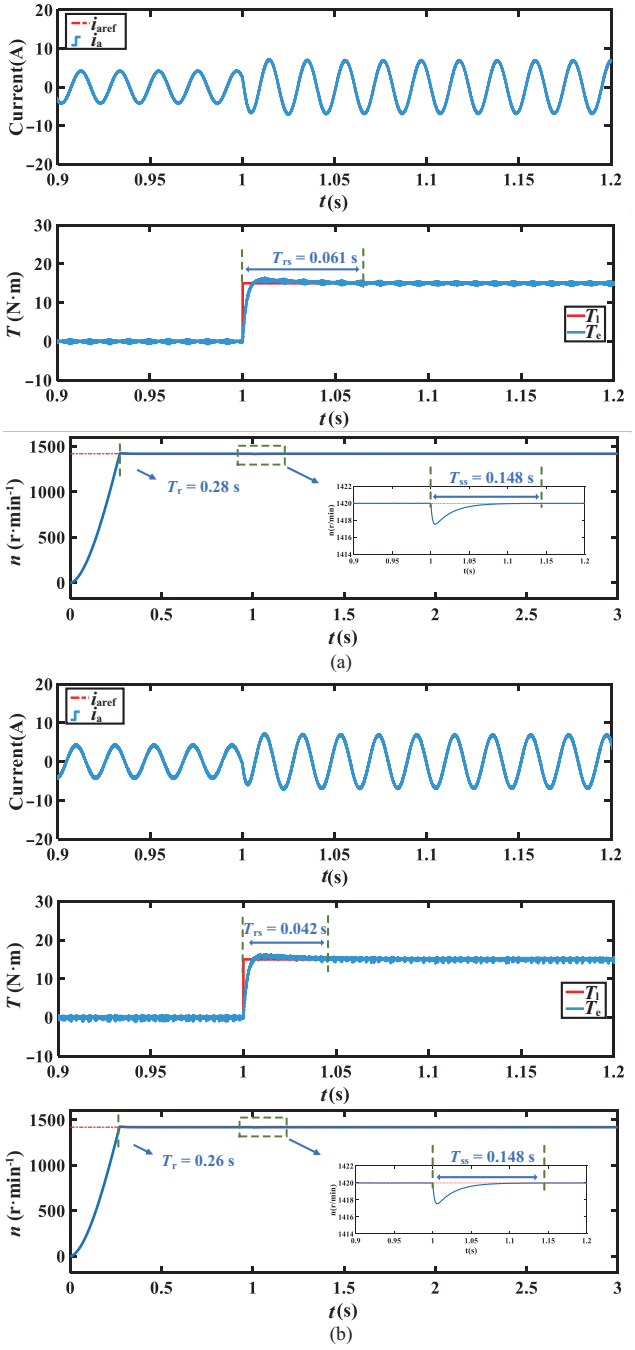

Fig. 9. Simulation comparison under light-load condition 1420 r/min, 15 N·m. (a) Traditional FCS-MPCC, (b) LVJ-SPI-MPCC.

and the speed fluctuation settling time by approximately 3.8%.

When operating at the rated speed of 1420 r/min, the motor was also started at no-load at 0 s and the rated load was applied at 1 s. The simulation comparison is shown in Fig. 8. Compared to traditional FCS-MPCC, LVJ-SPI-MPCC demonstrated improved tracking accuracy of the phase current to the reference current, with smoother and more stable waveforms, indicating superior performance in current control. The torque regulation time T_{rs} was 0.081 s for traditional FCS-MPCC but was reduced to 0.045 s with LVJ-SPI-MPCC. The speed rise time T_r was 0.31 s for traditional FCS-MPCC, which was shortened to 0.27 s with LVJ-SPI-MPCC. The speed fluctuation settling time after load application T_{ss} was reduced from 0.164 s to 0.152 s. Compared to traditional FCS-MPCC, LVJ-SPI-MPCC reduced the torque regulation time by approximately 44.4%, the speed rise time by 12.9%, and the speed fluctuation settling time by approximately 7.3%.

Furthermore, simulation analysis was conducted under light-load conditions at the rated speed with a 15 N·m load. When operating at the rated speed of 1420 r/min, the motor was started at no-load at 0 s, and a 15 N·m load was applied at 1 s. The simulation comparison is shown in Fig. 9. Compared

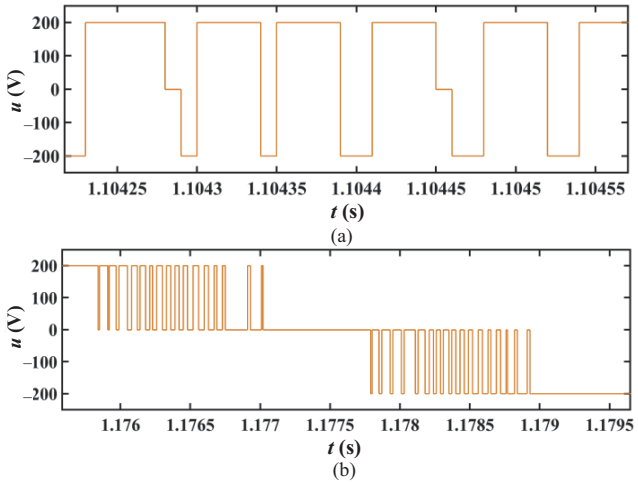

Fig. 10. Comparison of phase A voltage under rated condition. (a) SPI-MPCC, (b) LVJ-SPI-MPCC.

to traditional FCS-MPCC, LVJ-SPI-MPCC demonstrated improved tracking accuracy of the phase current relative to the reference current, with smoother and more stable waveforms. The torque regulation time T_{rs} was 0.061 s for traditional FCS-MPCC, while it was reduced to 0.042 s for LVJ-SPI-MPCC. Additionally, LVJ-SPI-MPCC exhibited smaller torque overshoot, enabling faster and more stable attainment of steady-state torque. The speed rise time T_r was 0.28 s for traditional FCS-MPCC, and the settling time after load application T_{ss} was 0.148 s. With LVJ-SPI-MPCC, T_r was shortened to 0.26 s, while T_{ss} remained unchanged at 0.148 s. Compared to traditional FCS-MPCC, LVJ-SPI-MPCC reduced the torque regulation time by approximately 31.1% and the speed rise time by 7.1%.

Fig. 10 presents a comparison of the phase A voltage under rated operating conditions for both methods. As can be observed from the figure, the phase voltage in SPI-MPCC exhibits jumps from $-U_{dc}/2$ to $U_{dc}/2$. In contrast, LVJ-SPI-MPCC incorporates a constraint condition that successfully suppresses each phase voltage jump to within $U_{dc}/2$.

In this paper, LVJ-SPI-MPCC is compared with traditional FCS-MPCC in stator resistance reduction by 50% and increase by 50% to verify the control performance of the proposed method. Fig. 11 analyzes the steady-state performance of driving OEWIM under different control modes by comparing the speed and torque waveforms when the stator resistance is reduced by 50%. Fig. 11 presents a comparative simulation of the conventional FCS-MPCC and the proposed LVI-SPI-MPCC under rated operating conditions. As shown in Fig. 11(a), the conventional FCS-MPCC exhibits a periodic speed oscillation of approximately ±0.011 r/min around the reference speed of 1420 r/min, with a mean electromagnetic torque tracking error of 1.3 N·m. In contrast, the system employing the proposed LVI-SPI-MPCC method demonstrates significantly improved steady-state performance. The speed ripple is suppressed to within 0.005 r/min, representing a reduction of 78.26% compared to the conventional method. Furthermore, the mean electromagnetic torque tracking error is reduced to 0.42 N·m, which is only 32.31% of that achieved

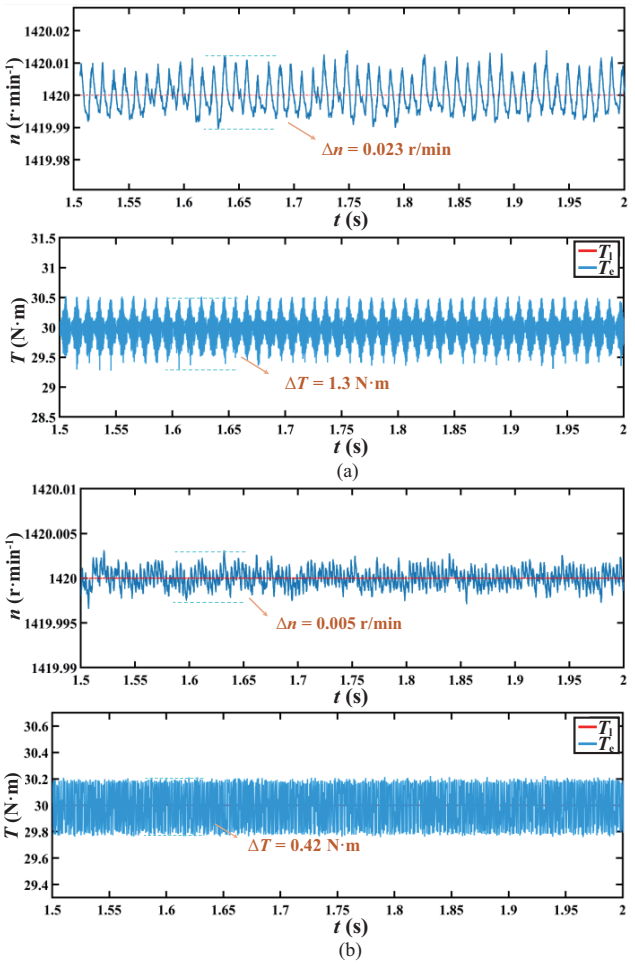

Fig. 11. Comparative simulation of tracking performance under 50% R_s variation. (a) Traditional FCS-MPCC, (b) LVJ-SPI-MPCC.

by the conventional scheme.

Fig. 11 compares the speed and torque waveforms of the conventional FCS-MPCC and the proposed LVI-SPI-MPCC for driving the OEWIM under a 50% increase in stator resistance, analyzing the steady-state performance of the system under different control strategies. The simulation results demonstrate that the conventional FCS-MPCC exhibits a steady-state speed error of approximately ±0.025 r/min around the reference speed of 1420 r/min, with a mean electromagnetic torque tracking error of 1.1 N·m. In contrast, the proposed LVI-SPI-MPCC method shows significantly improved robustness and steady-state accuracy. The speed fluctuation is suppressed within ±0.0048 r/min, representing an 80.8% reduction compared to the conventional method. Furthermore, the mean electromagnetic torque tracking error is reduced to 0.413 N·m, which is only 37.55% of that of the conventional scheme.

Simulation results demonstrate that, across various operating conditions, LVJ-SPI-MPCC exhibits superior current tracking performance as well as improved dynamic response in torque and speed compared to traditional FCS-MPCC.

B. Experimental Result Analysis

To verify the effectiveness of the proposed single-phase

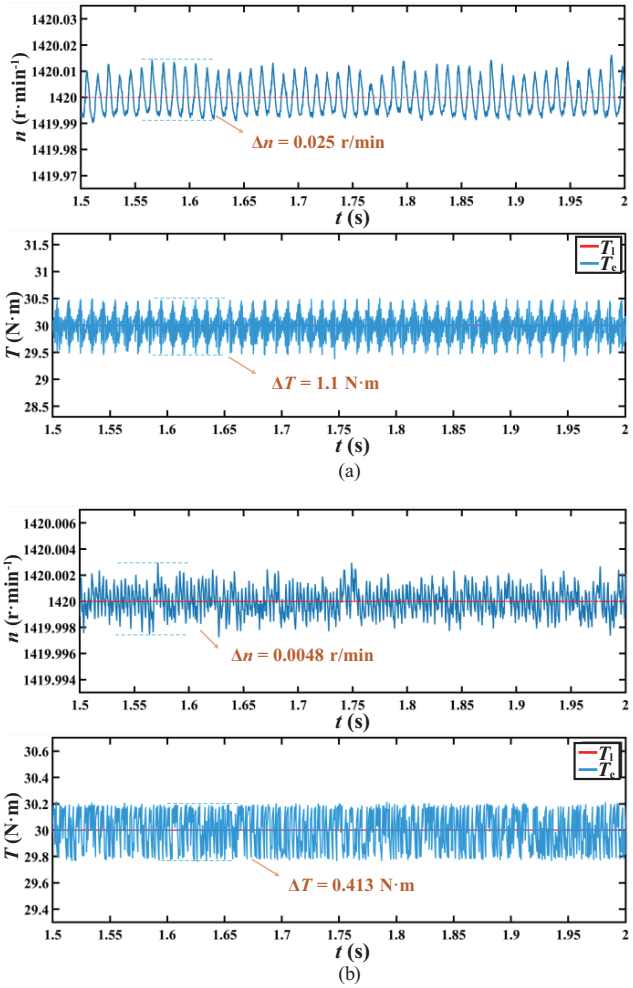

Fig. 12. Comparative simulation of tracking performance under 150% R_s variation. (a) Traditional FCS-MPCC, (b) Traditional FCS-MPCC.

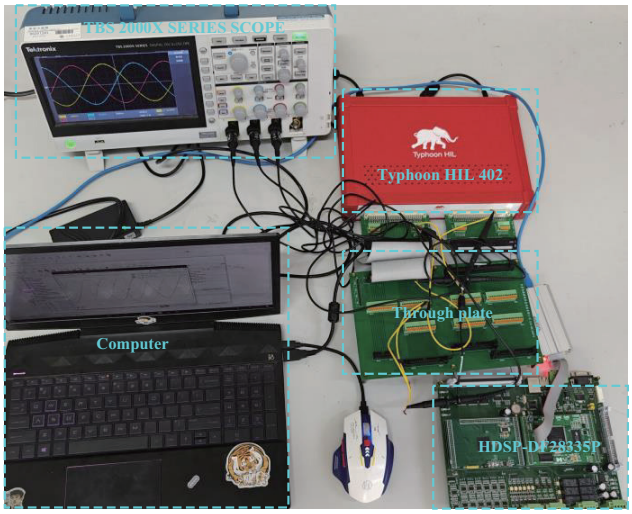

Fig. 13. Hardware-in-the-loop experimental platform.

independent model predictive control method for the OEWIM based on the dual three-level inverter, the hardware-in-the-loop experimental platform shown in Fig. 13 was built. In this platform, the main circuit model is built based on Typhoon

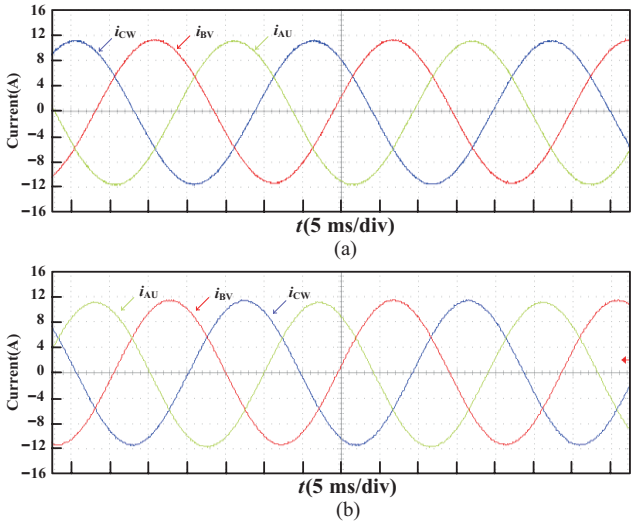

Fig. 14. Comparison of three-phase currents under rated conditions. (a) Traditional FCS-MPCC, (b) LVJ-SPI-MPCC.

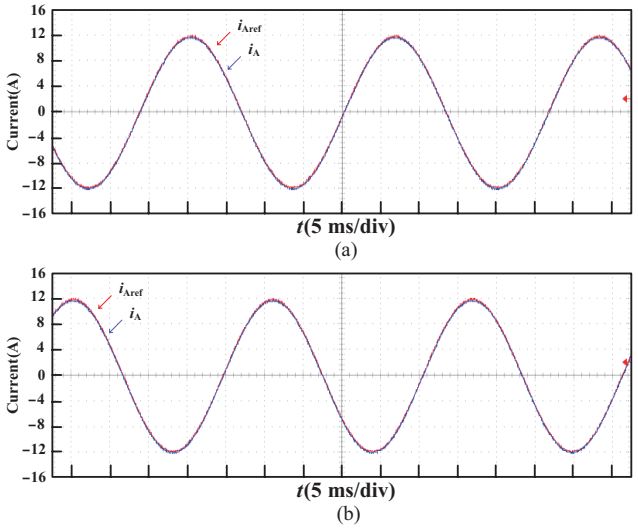

Fig. 15. Comparison of phase A current tracking effect under rated conditions. (a) Traditional FCS-MPCC, (b) LVJ-SPI-MPCC.

HIL 402, and the output pulses are generated by the HDSP-DF28335P controller. To ensure the reliability and consistency of the experimental results, the relevant parameter settings are consistent with the simulation section.

Fig. 14 shows the comparison of three-phase currents under rated conditions for both methods. The phase relationships of the three-phase currents are basically correct under both methods, without significant phase drift. However, under traditional FCS-MPCC, there are certain fluctuations compared to LVJ-SPI-MPCC. Under LVJ-SPI-MPCC, the three-phase current waveforms are smoother and more stable, indicating better performance in current control, effectively reducing current pulsation during motor operation, and improving motor operating efficiency and stability.

Fig. 15 shows the comparison of phase A current tracking performance under rated conditions for both methods. It can be seen that due to the lower computational load of LVJ-SPI-MPCC, it can respond to current changes faster. The actual

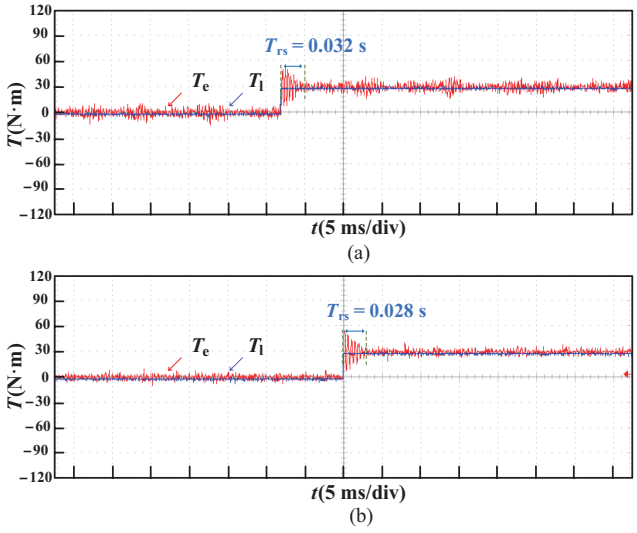

Fig. 16. Comparison of output torque under rated conditions. (a) Traditional FCS-MPCC, (b) LVJ-SPI-MPCC.

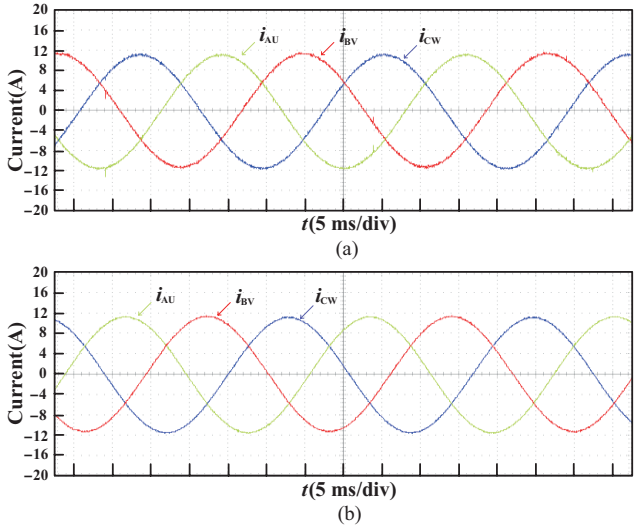

Fig. 17. Comparison of three-phase currents under medium-speed condition 1000 r/min. (a) Traditional FCS-MPCC, (b) LVJ-SPI-MPCC.

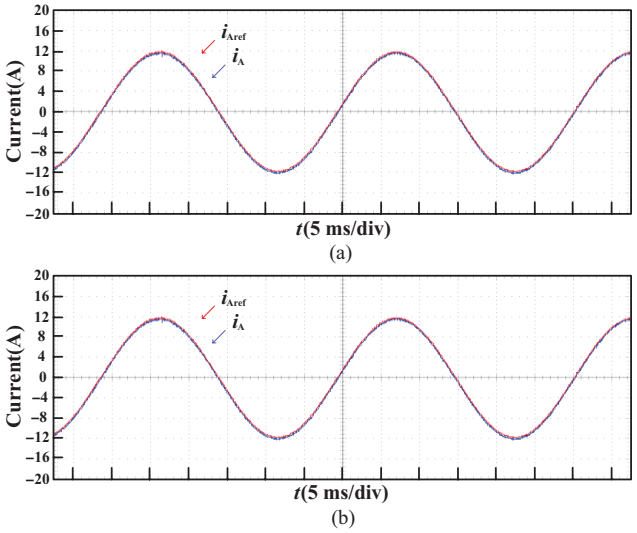

Fig. 18. Comparison of Phase A current tracking effect under medium-speed condition 1000 r/min. (a) Traditional FCS-MPCC, (b) LVJ-SPI-MPCC.

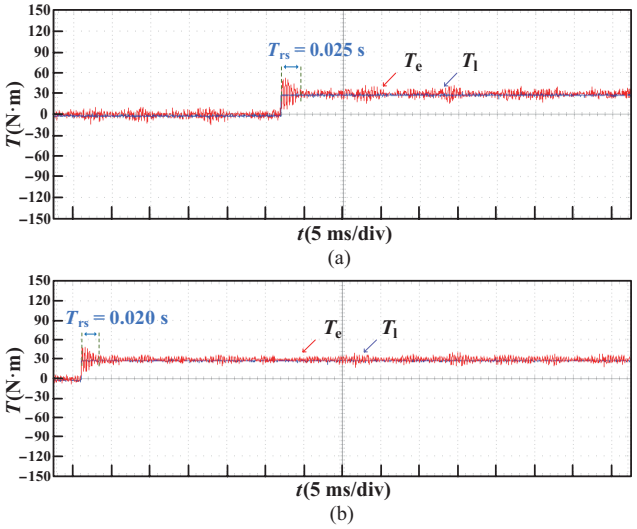

Fig. 19. Comparison of output torque under medium-speed condition 1000 r/min. (a) Traditional FCS-MPCC, (b) LVJ-SPI-MPCC.

current matches the reference current more closely, with smaller deviation.

Fig. 16 shows the output torque comparison under rated conditions for traditional FCS-MPCC and LVJ-SPI-MPCC. Under traditional FCS-MPCC, the torque rise time T_{rs} is 0.032 s, while under LVJ-SPI-MPCC, the torque rise time is shortened to 0.028 s, a reduction of about 12.5%. Under traditional FCS-MPCC, the torque fluctuation amplitude is larger, and the curve is less smooth. Under LVJ-SPI-MPCC, the torque fluctuation amplitude is significantly reduced, and the curve is smoother, indicating better performance in torque control, effectively reducing torque ripple, and improving the smoothness of motor operation.

Fig. 17 shows the comparison of three-phase currents under medium-speed condition for both methods. The phase relationships of the three-phase currents are basically correct under both methods, without significant phase drift. However, under traditional FCS-MPCC, there are certain fluctuations compared to LVJ-SPI-MPCC. Under LVJ-SPI-MPCC, the three-phase current waveforms are smoother and more stable, indicating better performance in current control, effectively reducing current pulsation during motor operation, and improving motor operating efficiency and stability.

Fig. 18 shows the comparison results of phase A current tracking under medium-speed condition. Thanks to the simplification of LVJ-SPI-MPCC algorithm structure and the reduction of calculation load, its response speed to the current command is significantly better than that of the traditional scheme; the actual current waveform is almost coincident with the reference value, and the steady-state error and dynamic deviation are compressed to a minimum, which fully verifies the advantages of the method in tracking accuracy and response agility.

Fig. 19 compares the output torque characteristics of

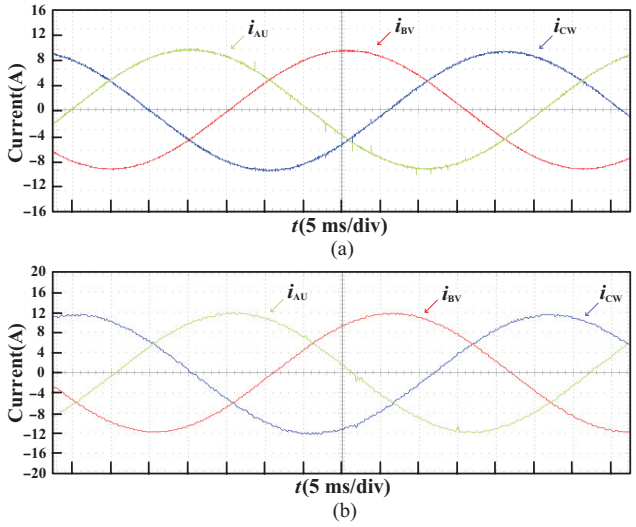

Fig. 20. Comparison of three-phase currents under low-speed condition 500 r/min. (a) Traditional FCS-MPCC, (b) LVJ-SPI-MPCC.

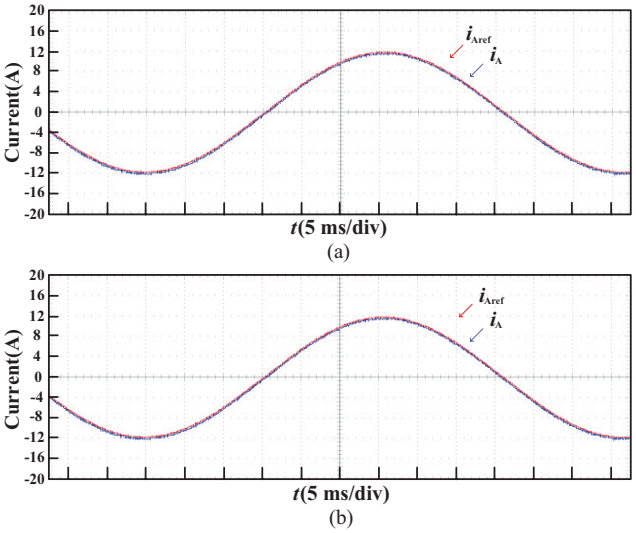

Fig. 21. Comparison of phase A current tracking effect under low-speed condition 500 r/min. (a) Traditional FCS-MPCC, (b) LVJ-SPI-MPCC.

conventional FCS-MPCC and LVJ-SPI-MPCC at medium-speed condition. The torque rise time T_{rs} of the traditional scheme is 0.025 s, while that of LVJ-SPI-MPCC is shortened to 0.020 s, and the speed is increased by about 25%. At the same time, the torque ripple of traditional control is significant and the curve fluctuation is obvious, while the torque waveform of LVJ-SPI-MPCC is smoother and the ripple amplitude is greatly reduced, which reflects better torque control accuracy and dynamic response quality, effectively suppresses the torque ripple, and significantly improves the stability and reliability of motor operation.

Fig. 20 presents the comparison results of three-phase currents under low-speed condition for the two control strategies. It can be seen that both schemes maintain the correct phase relationship without any noticeable phase drift. However, the current waveform of the traditional FCS-MPCC shows obvious fluctuations, while the current curve of the LVJ-SPI-MPCC is smoother and more stable. This phenomenon indicates that the proposed LVJ-SPI-MPCC method performs better in terms of current tracking accuracy and ripple suppression, effectively reducing the current harmonics during motor operation and significantly improving the system's operational efficiency and electromechanical stability.

Fig. 21 shows the phase A current tracking results at low-speed condition. Thanks to the significant simplification of LVJ-SPI-MPCC algorithm structure and computational burden, its dynamic response speed is improved. Compared with the traditional scheme, the current tracking error of the proposed method is smaller, and the current drop in the dynamic process is also less, which verifies its effectiveness in improving the dynamic response and steady-state accuracy.

Fig. 22 compares the output torque characteristics of traditional FCS-MPCC and LVJ-SPI-MPCC under low-speed condition. The rising time T_{rs} of traditional control torque is 0.059 s, while that of LVJ-SPI-MPCC is only 0.045 s, and the dynamic response speed is increased by about 31.1%, which verifies its advantages in dynamic response.

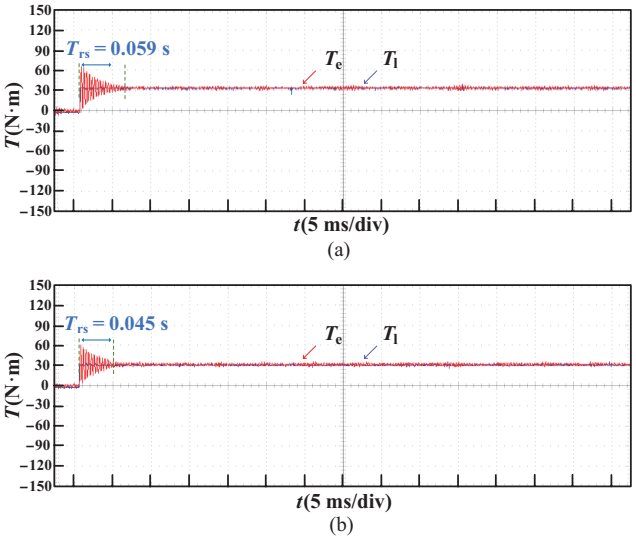

Fig. 22. Comparison of output torque under low-speed condition 500 r/min. (a) Traditional FCS-MPCC, (b) LVJ-SPI-MPCC.

Fig. 23 shows the average computation time for FCS-MPCC and LVJ-SPI-MPCC, respectively. The average computation time for FCS-MPCC is 79.27 μs. The average computation time for LVJ-SPI-MPCC is 24.88 μs. Compared to MPCC, the proposed LVJ-SPI-MPCC reduces computation time by 54.39 μs, and the overall computation speed is increased by approximately 2.186 times.

In comprehensive comparison, the proposed LVJ-SPI-MPCC has stronger static and dynamic stability capabilities compared to traditional FCS-MPCC, better output current waveform quality, and effectively reduces the computational load on the controller, improving system efficiency and response speed.

V. Conclusion

This paper proposed a low voltage jump single-phase

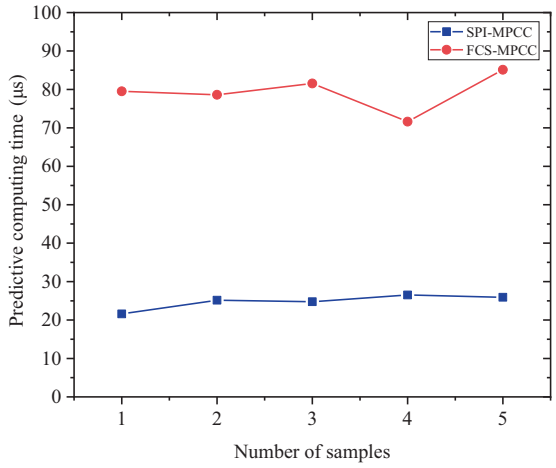

Fig. 23. Comparison of computation time.

independent model predictive current control (LVJ-SPI-MPCC) method for open-end winding induction motors based on an isolated DC-bus dual three-level inverter. By incorporating the idea of single-phase independent control, a single-phase current independent predictive mathematical model was established, achieving independent prediction and optimization of the switching states for each phase leg. This reduced the number of predictive computations for the optimal switching state per control cycle from 729 to 27. A switching state selection rule based on voltage jump constraints was proposed, constructing a collaborative optimization strategy for low voltage jump and single-phase independent control. This limited the phase voltage jump within $\pm U_{dc}/2$ and further reduced the number of optimal switching state predictive computations to 15 per cycle, improving system response speed. Experimental and simulation results showed that compared to the traditional FCS-MPCC method, the proposed method improved torque regulation speed by 44.4%, reduced speed rise time by 12.9%, and reduced speed fluctuation adjustment time by about 7.3% during steady-state operation under rated conditions. This fully verifies the superiority and effectiveness of the proposed LVJ-SPI-MPCC method in reducing computational burden and improving system dynamic response speed.

References

[1] N. R. Kedika and S. Pradabane, "Floating-capacitor based inverter for open-ended winding induction motor drive with fault-tolerance," in *International Journal of Electronics*, vol. 110, no. 8, pp. 1468–1490, 2023.

[2] Y. Jia , A. Wang , Q. Zhang, and N. Xu, "Power allocation-oriented stator current optimization and dynamic control of a dual-inverter open-winding PMSM drive system for dual-power electric vehicles," in *Energy*, vol. 322, pp. 135587, May 2025.

[3] B. Wang, X. Zhang, and R. Cao, "A zero-sequence steerable CBPWM strategy for eliminating zero-sequence current of dual-inverter fed open-end winding transformer based PV grid-tied system with common DC bus," in *IEEE Access*, vol. 8, pp. 81220–81231, 2020.

[4] D. Casadei, G. Grandi, A. Lega, and C. Rossi, "Multilevel operation and input power balancing for a dual two-level inverter with insulated DC sources," in *IEEE Transactions on Industry Applications*, vol. 44, no. 6, pp. 1815–1824, Nov.-Dec. 2008.

[5] A. Paramasivam, D. Kalaiyarasi, M. S. Raja, and R. Pavaiyarkarasi, "An efficient COA approach-based open-end winding induction motor with direct torque control for minimize the power loss," in *Electrical Engineering*, vol. 107, pp. 20735–2087, 2025.

[6] T. Kawabata, E. C. Ejiogu, Y. Kawabata, and K. Nishiyama, "New open-winding configurations for high-power inverters," in *ISIE '97 Proceeding of the IEEE International Symposium on Industrial Electronics, Guimaraes, Portugal,* vol. 2, pp. 457–462, 1997.

[7] J. -H. Park, H. -W. Choi, and K. -B. Lee, "Analysis and suppression of zero-sequence circulating current in parallel three-level inverters using improved interleaved DPWM," in *2022 International Power Electronics Conference (IPEC-Himeji 2022- ECCE Asia)*, Himeji, Japan, 2022, pp. 845–848.

[8] J. -H. Park, H. -W. Choi, and K. -B. Lee, "Improved integrated modulation strategy for dual-parallel three-level inverters to suppress leakage currents," in *IEEE Transactions on Power Electronics*, vol. 39, no. 1, pp. 898–910, Jan. 2024.

[9] Y. Liu, W. Li, Y. Jia, M. Luo, and S. Zhang, "Three-level control for open winding permanent magnet synchronous motors," in *Journal of Physics: Conference Series,* vol. 2849, no. 1, pp. 12010, 2024.

[10] D. Sun, W. Chen, Y. Cheng, and H. Nian, "Improved direct torque control for open-winding PMSM system considering zero-sequence current suppression with low switching frequency," in *IEEE Transactions on Power Electronics*, vol. 36, no. 4, pp. 4440–4451, Apr. 2021.

[11] P. Cataldo, W. Jara, J. Riedemann, and C. P. G., "A predictive current control strategy for a medium-voltage open-end winding machine drive", in *Electronics,* vol. 12, no. 5, pp. 1070, Feb. 2023.

[12] H. Yang, Y. Yi, F. Fu, Z. Zhu, and H. Lin, "State-of-the-art and future trends of zero-sequence current excited machines: drive topology and control technologies," in *Transactions of China Electrotechnical Society,* vol. 40, no. 2, pp. 398–414, 2025.

[13] Z. Liu, Y. Li, Z. Zheng, "Control and drive techniques for multiphase machines: a review," in *Transactions of China Electrotechnical Society,* vol. 32, no. 24, pp. 17–29, Dec. 2017.

[14] M. Preindl and S. Bolognani, "Model predictive direct torque control with finite control set for PMSM drive systems, part 1: maximum torque per ampere operation," in *IEEE Transactions on Industrial Informatics*, vol. 9, no. 4, pp. 1912–1921, Nov. 2013.

[15] D. Sun and X. Wang, "Low-complexity model predictive direct power control for DFIG under both balanced and unbalanced grid conditions," in *IEEE Transactions on Industrial Electronics*, vol. 63, no. 8, pp. 5186–5196, Aug. 2016.

[16] W. Xie, X. Wang, F. Wang, W. Xu, R. M. Kennel, D. Gerling, and R. D. Lorenz, "Finite-control-set model predictive torque control with a deadbeat solution for PMSM drives," in *IEEE Transactions on Industrial Electronics*, vol. 62, no. 9, pp. 5402–5410, Sept. 2015.

[17] R. E. Kodumur Meesala, V. P. K. Kunisetti, and V. Kumar Thippiripati, "Enhanced predictive torque control for open end winding induction motor drive without weighting factor assignment," in *IEEE Transactions on Power Electronics*, vol. 34, no. 1, pp. 503–513, Jan. 2019.

[18] D. Wu, J. Chen, R. Zhu, and G. Hua, "Simplified model predictive flux control for dual inverter fed open end winding induction motor," in *2019 IEEE 10th International Symposium on Power Electronics for Distributed Generation Systems (PEDG)*, Xi'an, China, 2019, pp. 1050–1054.

[19] W. Wang, Y. Fan, S. Chen, and Q. Zhang, "Finite control set model predictive current control of a five-phase PMSM with virtual voltage vectors and adaptive control set," in *CES Transactions on Electrical Machines and Systems*, vol. 2, no. 1, pp. 136–141, Mar. 2018.

[20] F. Ban,G. Lian, G. Gu, H. Ye, and H. Ding, "Research on single vector decoupling model predictive torque control strategy for PMSM," in *Advanced Technology of Electrical Engineering and Energy,* vol. 39, no. 12, pp. 44–51, 2020.

[21] X. Wu, W. Song, and C. Xue, "Low-complexity model predictive torque control method without weighting factor for five-phase PMSM based on hysteresis comparators," in *IEEE Journal of Emerging and Selected Topics in Power Electronics*, vol. 6, no. 4, pp. 1650–1661, Dec. 2018.

[22] Z. Feng, L. Gao, K. Yin, and W. Fu, "Improved model predictive zero vector injection control for open-winding permanent magnet synchronous motors," in *Electric Machines and Control,* vol. 26, no. 2, pp. 32–42, 2022.

[23] S. Lakhimsetty and V. T. Somasekhar, "An efficient predictive current

control strategy for a four-level open-end winding induction motor drive," in *IEEE Transactions on Power Electronics*, vol. 35, no. 6, pp. 6198–6207, Jun. 2020.

[24] F. Gao, Y. Wu, H. Xu, Z. Shi, W. Yue, W. Sun, and G. Wang, "Common bus bar open winding permanent magnet synchronous traction motors cascade model predictive current control," in *Journal of Railway Science and Engineering,* vol. 21, no. 8, pp. 3321–3334, 2024.

[25] N. S. P. Musunuru and S. Srirama, "A fast model predictive control method for a single DC source driven dual inverter fed open-end winding induction motor drive," in *Electric power components and systems,* vol. 50, no. 16-17, pp. 899–915, 2022.

[26] Q. Yuan, F. Bu, X. Xie, and K. Xia, "Improved model predictive voltage control for the NPC three-level dual three-phase PMSM based on vectors' classification," in *Proceedings of the CSEE,* vol. 45, no. 2, pp. 758–768, 2025.

Chao Luo was born in Taizhou, China, in 2001. He received the B.S. degree in electrical engineering and automation from Nanjing Tech University, China, in 2023. He is currently working toward the M.S. degree in electronic information with Jiangsu Normal University, Xuzhou, China.His current research interests lie in the fields of power electronics and electric machine drives.

Guifeng Wang was born in Linyi, Shandong, China, in 1982. He obtained his B.S. degree in electrical engineering and automation and M.S. degree in electrical engineering from the School of Information and Electrical Engineering, China University of Mining and Technology, Xuzhou, China, in 2004 and 2007, respectively. In 2016, he was awarded a Ph.D. in power electronics and electrical drive from Shanghai Jiao Tong University, Shanghai, China. Currently, Dr. Wang holds the position of Senior Engineer at the College of Electrical Engineering and Automation, Jiangsu Normal University, Xuzhou. His research primarily focuses on power electronic converters for electrical drives and power quality enhancement.

Qigang Du was born in Xuzhou, China, in 2002. He received the B.S. degree in electrical engineering and automation from Changchun Institute of Technology, Changchun, China, in 2022. He is currently working toward the M.S. degree in electronic information with Jiangsu Normal University, Xuzhou, China.His current research interests include model predictive control, power conversion, and power quality.

Jinling Ji was born in FuYang, China， in 2001. She received the B.S. degree in electrical engineering and automation from Xi'an University of Technology, Xi'an, China, in 2022. She is currently pursuing the M.S. degree in electrical engineering with Jiangsu Normal University, Xuzhou, China. Her research interests include model predictive control and hybrid AC/DC output.

Weipeng Shi received the Ph.D. degree from Southeast University, Nanjing, China, in 2024. He is currently a Lecturer withthe School of Electrical Engineering and Automation, Jiangsu Normal University, Xuzhou, China. His research interests include computer vision, remote sensing detection, and fundamental theory and applications of artificial intelligence.

Ke Li works as an electrical motor R&D engineer at South-Power Electromechanical Technology Co., Ltd., Xuzhou, China. His research interests include AC motors, permanent magnet synchronous motor control, and related drive technologies.